

This is a self-archived version of an original article. This version may differ from the original in pagination and typographic details.

Author(s): Rautiainen, J. Mikko; Green, Maryna; Mähönen, Minna; Moilanen, Jani O.;
Lahtinen, Manu; Valkonen, Arto

Title: Halogen-Bonded Mono-, Di-, and Tritopic N-Alkyl-3-iodopyridinium Salts

Year: 2023

Version: Published version

Copyright: © The Authors. Published by American Chemical Society

Rights: CC BY 4.0

Rights url: <https://creativecommons.org/licenses/by/4.0/>

Please cite the original version:

Rautiainen, J. M., Green, M., Mähönen, M., Moilanen, J. O., Lahtinen, M., & Valkonen, A. (2023). Halogen-Bonded Mono-, Di-, and Tritopic N-Alkyl-3-iodopyridinium Salts. *Crystal Growth and Design*, 23(4), 2361-2374. <https://doi.org/10.1021/acs.cgd.2c01351>

Halogen-Bonded Mono-, Di-, and Tritopic *N*-Alkyl-3-iodopyridinium Salts

J. Mikko Rautiainen, Maryna Green, Minna Mähönen, Jani O. Moilanen,* Manu Lahtinen, and Arto Valkonen*

Cite This: <https://doi.org/10.1021/acs.cgd.2c01351>

Read Online

ACCESS |



Metrics & More

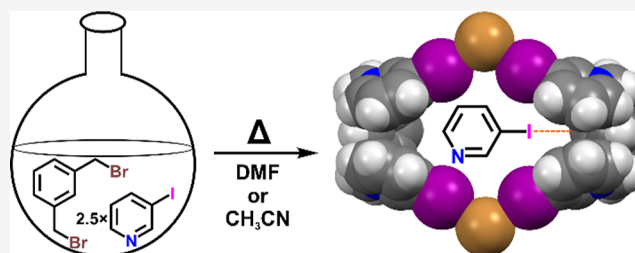


Article Recommendations



Supporting Information

ABSTRACT: Halogen bonding interactions of 15 crystalline 3-iodopyridinium systems were investigated. These systems were derived from four *N*-alkylated 3-iodopyridinium salts prepared in this study. The experimental results in the solid state show that halogen bonding acts as a secondary intermolecular force in these charged systems but sustains the high directionality of interaction in the presence of other intermolecular forces. Halogen bonds donated by polytopic 3-iodopyridinium cations are also sufficient to enclose guest molecules inside the formed supramolecular cavities. The experimental data were supplemented by computational gas-phase and solid-state studies for selected halogen-bonded systems. Calculations of the model systems with the increasing number of halogen bond donors and acceptors showed the halogen bond strengths to be exaggerated for the smallest of model systems. The agreement between experimental and calculated structures improved for larger systems that were able to account for the influence of other intermolecular interactions. The best agreement between experimental and calculated structural parameters were found for solid-state calculations with periodic boundary conditions. Comparison of the halogen bond interaction strengths with the strength of other lattice interactions showed the halogen bonds to come second to electrostatic interactions in stabilizing the structures but having a major role in directing the packing of the solid-state structures.



1. INTRODUCTION

The halogen bonding (XB)¹ story is considered to have begun around 200 years ago,^{2,3} but XB has started to invoke extensive research interest only during the last quarter of a century^{4–8} and is still a rapidly developing research topic in the fields of structural, biological, and supramolecular chemistry. Most of the XB research has concentrated on strong interactions, which utilize strong halogen bond donors, like dihalogens,^{3,9–11} perfluorohalocarbons,^{6–8,12–14} N–X donors,^{15–17} or halonium (X⁺) ions,^{18–22} and strong nucleophilic acceptors. This contrasts with the XB systems found in the nature where such strong donors are scarce, while plenty of good acceptors exist.²³ For the research aiming to gain a better understanding of XB in biological systems, including the interactions of halogenated drugs and persistent organic pollutants as well as naturally halogenated hormones and amino acids, it would be best to employ systems with intermediate donor strengths in model studies. One rather simple halogen bond donor unit that falls in this category is the 3-iodopyridine (3IPy) moiety, which was selected as the focus of the study.

The 3IPy unit has been occasionally shown to act as a halogen bond donor (D) in solid-state supramolecular systems. Regardless of the acceptor (A), it is able to form remarkably short interatomic D...A distances with normalized interaction ratios R_{XB} down to 0.80 and with relatively straight XB angles

\angle_{XB} ($>160^\circ$).²⁴ Neutral 3IPy usually forms XB contacts, which are of similar length to the I...O in 2-benzoyl-3IPy (R_{XB} : 0.90)²⁵ or I...N between 3IPy-ligands and cyanide ligands (R_{XB} : 0.88) in the $[\text{Cu}^{\text{II}}(3\text{IPy})_4][\text{Cu}^{\text{II}}(3\text{IPy})_2][\text{W}^{\text{V}}(\text{CN})_8]_2$ assembly.²⁶ However, a few shorter I...N XB distances have been found, like in the polymorphic structure of 2-benzoyl-3IPy (R_{XB} : 0.85)²⁵ and in 4-(5-iodo-1*H*-pyrazol-1-yl)-3IPy (R_{XB} : 0.84).²⁷

Compared to the neutral donor, charged 3IPy⁺ units have recently gained more research interest.^{28–32} It has been reported that 3IPy⁺ units can bind halides forming mono-, di-, and tritopic binding motifs and highly directional C–I...X interactions, in which R_{XB} values are 0.83–0.85^{33,34} for Cl[–], 0.84–0.91^{28,30,34} for Br[–], and 0.85–0.91^{28,30,31,34} for I[–] acceptors (\angle_{XB} : 163–180°). For example, *N*-methyl-3-iodopyridinium cations (*N*-Me-3IPy⁺) interact with $\{[\text{Ru}(\text{bipy})(\text{CN})_4]^{2-}\}^{35}$ and $[\text{M}(\text{CN})_6]^{3-}$ (M = Cr, Fe, and Co) complex anions³⁶ through C–I...N halogen bonds with R_{XB}

Received: November 17, 2022

Revised: February 17, 2023

(\angle_{XB}) values of 0.80–0.84 (171–179°) and 0.82–0.88 (166–174°), respectively. Furthermore, mono- and ditopic C–I...O halogen bonds to oxyanions have been reported between 1,3,5-tris((3IPy⁺)methyl)-2,4,6-trimethylbenzene and NO₃[−] (R_{XB} : 0.84, \angle_{XB} : 178°),³⁷ 4,4'-(1,3-phenylenebis(ethyne-2,1-diyl))-bis(*N*-Me-3IPy⁺) and CF₃SO₃[−] (R_{XB} : 0.82, \angle_{XB} : 169°),³⁴ and 2,2'-bis(*N*-Me-3IPy⁺) and HSO₄[−] (R_{XB} : 0.80, \angle_{XB} : 162°).²⁹ The 3IPy⁺ unit also forms halogen bonds with neutral acceptors, like C–I...O between the 1,3,5-tris((3IPy⁺)methyl)-2,4,6-tris(*n*-hexyloxy)benzene trication and solvent MeOH (R_{XB} : 0.81, \angle_{XB} : 177°).²⁸

Above examples along with the data in the Cambridge Structural Database (CSD, total 251 hits)³⁸ including very recent studies by Stilić and co-workers^{30–32} show that the cationic 3IPy⁺ unit is more common and usually a stronger halogen bond donor than the neutral 3IPy moiety. However, halogen bonds in 3IPy⁺ systems can be considered secondary interactions due to the strong attractive ionic forces dominating the crystal packing. Albeit auxiliary in character, the halogen bonds are very important for the structure, properties, and potential exploitability of the complexes. This and our diverse interest in the XB interactions^{9,10,17,20,39–41} led us to perform a further study on 3IPy⁺ structures. One of our targets is to find XB systems with anion sensing capabilities in organic solutions that could be extended to aqueous media.

Here, we prepared four 3IPy⁺ derivatives as halide salts and studied the products by NMR, mass spectrometry (MS), powder X-ray diffraction (PXRD), and thermogravimetry/differential scanning calorimetry (TG/DSC) analyses. Further crystallization experiments using different solvents, counter anions, and co-crystallization species were performed for these mono-, di-, and tritopic 3IPy⁺ derivatives to obtain crystalline materials for single crystal X-ray diffraction (SCXRD) measurements and to shed light on their XB interactions. The experimental results were complemented by density functional theory (DFT) calculations on gas-phase model systems of increasing sizes and solid-state calculations with periodic boundary conditions. By combining the results from the gas-phase and solid-state calculations, we were able to analyze the relative contribution of halogen bonds and other intermolecular interactions to the total interaction energies of three systems.

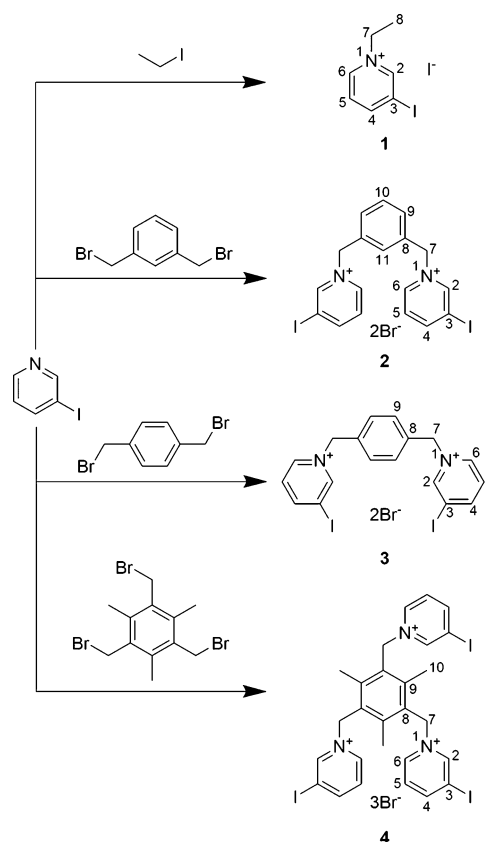
2. EXPERIMENTAL SECTION

2.1. Materials. The compounds prepared in this study are presented in Scheme 1. All commercial reagents (purity ≥ 97%) were used as received. Organic solvents were dried over molecular sieves (3 Å) before use. Only deionized water was used.

2.1.1. Preparation of 1. 3IPy (0.300 g, 1.46 mmol) was weighed into a flask and dissolved in 25 mL of CH₃CN. Iodoethane (0.34 g, 0.18 mL, 2.20 mmol) was added by a syringe into the solution. The resulting solution was refluxed for 4 h. The still hot solution was poured into 100 mL of cold diethyl ether. The resulting pale-yellow product was collected by filtration and dried under high vacuum. Yield: 0.45 g (86%), m.p. 136 °C. ¹H NMR (500 MHz, D₂O): δ 9.32 (s, 1H, H2), 8.93–8.97 (m, 2H, H4 & H6), 7.90 (t, *J* = 6.7 Hz, 1H, H5), 4.68 (q, *J* = 7.3 Hz, 2H, H7), 1.70 (t, *J* = 7.3 Hz, 3H, H8) ppm. ¹³C NMR (126 MHz, D₂O): δ 153.4 (C4), 149.5 (C2), 142.7 (C6), 128.3 (C5), 93.6 (C3), 57.2 (C7), 15.4 (C8) ppm. NMR data show good correspondence with the data of 3-iodo-*N*-butylpyridinium hexafluorophosphate in DMSO-*d*₆.⁴² MS: *m/z* = 233.97 [M – I]⁺.

2.1.2. Preparation of 2. α,α'-Dibromo-*m*-xylene (0.26 g, 1.00 mmol) and 3IPy (0.51 g, 2.50 mmol) were weighed into a flask and dissolved in 25 mL of dimethylformamide (DMF). The resulting mixture was heated overnight at 85 °C. The white precipitate that

Scheme 1. Syntheses of Compounds 1–4 and Atom Numbering



formed in the reaction was filtered, washed with hot CHCl₃, and dried under high vacuum. Yield: 0.22 g (28%, with respect to **2d**, see below). ¹H NMR (500 MHz, D₂O): δ = 9.30 (s, 2H, H2), 8.96–9.00 (m, 4H, H4 & H6), 7.90 (t, *J* = 7.2 Hz, 2H, H5), 7.57–7.67 (m, 4H, H9 & H10 & H11), 5.86 (s, 4H, H7) ppm. ¹³C NMR (126 MHz, D₂O): δ = 154.2 (2C, C4), 149.7 (2C, C2), 143.2 (2C, C6), 133.4 (2C, C8), 130.5 (C10), 130.3 (2C, C9), 129.0 (C11), 128.4 (2C, C5), 93.7 (2C, C3), 63.7 (2C, C7) ppm. The extra 3IPy resonances in the spectra are discussed below and in the Supporting Information. MS: *m/z* = 256.89 [M – 2Br]²⁺.

2.1.3. Preparation of 3. α,α'-Dibromo-*p*-xylene (0.26 g, 1.00 mmol) and 3IPy (0.51 g, 2.50 mmol) were weighed into a flask and dissolved in 25 mL of DMF. The resulting mixture was heated overnight at 85 °C. The white precipitate that formed was filtered and dried under high vacuum. Yield: 0.55 g (83%). ¹H NMR (500 MHz, D₂O): δ 9.31 (s, 2H, H2), 8.95–9.00 (m, 4H, H4 & H6), 7.87–7.91 (m, 2H, H5), 7.60 (s, 4H, H9), 5.87 (s, 4H, H7) ppm. ¹³C NMR (126 MHz, D₂O): δ 154.2 (2C, C4), 149.7 (2C, C2), 143.2 (2C, C6), 133.8 (2C, C8), 129.8 (4C, C9), 128.4 (2C, C5), 93.5 (2C, C3), 63.6 (2C, C7) ppm. MS: *m/z* = 256.89 [M – 2Br]²⁺.

2.1.4. Preparation of 4. 1,3,5-Tris(bromomethyl)-2,4,6-trimethylbenzene (0.20 g, 0.50 mmol) and 3IPy (0.41 g, 2.0 mmol) were weighed into a flask and dissolved in 25 mL of CH₃CN. The resulting mixture was heated overnight at 85 °C. The yellow precipitate that formed was filtered, washed with hot CHCl₃, and dried under high vacuum. Yield: 0.31 g (87%). ¹H NMR (500 MHz, D₂O): δ = 9.08 & 9.15 (2 × s, 3H, H2), 8.95–9.00 (m, 3H, H4), 8.66 & 8.72 (2 × d, *J* = 5.7 Hz, 3H, H6), 7.84–7.91 (m, 3H, H5), 6.08 & 6.13 (2 × s, 6H, H7), 2.37 & 2.40 (2 × s, 9H, H10). ¹³C NMR (126 MHz, D₂O): δ = 154.4 & 154.6 (3C, C4), 149.0 (3C, C2), 144.6 (3C, C8), 142.0 (3C, C6), 128.8 & 129.0 (3C, C5), 128.2 (3C, C9), 94.2 & 94.4 (3C, C3), 59.2 & 59.4 (3C, C7), 16.5 (3C, C10). Some impurity resonances were observed in the spectra (see the discussion below and Supporting Information). MS: *m/z* = 257.99 [M – 3Br]³⁺. These

NMR and MS data show good correspondence with the data of the corresponding tris(hexafluorophosphate) salt.³⁷

2.2. Crystallizations. Crystallization attempts were performed by dissolving the materials in common solvents in test tubes. The tubes were closed with caps and left to stand at room temperature. The crystals suitable for SCXRD experiments were obtained from the solutions or found in the completely evaporated residues. Crystals of **2a** were obtained from an NMR sample of product **2** (in D₂O) upon standing at room temperature for 2 weeks.

2.3. Analytical Methods. **2.3.1. NMR Spectroscopy.** The NMR spectra were recorded with a Bruker AVANCE DRX 500 FT-NMR spectrometer at 303 K. The chemical shifts are reported in parts per million and referenced for ¹H spectra using the standard residual D₂O resonances relative to tetramethylsilane (δ = 4.80 ppm). The NMR spectra are presented in the [Supporting Information](#) (Figures S1–S20).

2.3.2. Mass Spectrometry. MS measurements of the synthetic products were performed with ABSciex QSTAR ESI-QTOF (**1** and **4**) and Micromass LCT ESI-TOF (**2** and **3**) mass spectrometers. Recorded MS spectra are shown in the [Supporting Information](#) (Figures S21–S24).

2.3.3. Single Crystal X-ray Diffraction. Crystallographic data (except for **1c**, **4a**, and **4b**) were collected with a Bruker Nonius KappaCCD diffractometer (APEX II detector) using graphite monochromatized Mo K α radiation (λ = 0.71073 Å). COLLECT⁴³ data collection and DENZO-SMN⁴⁴ data processing software were utilized. Data for **1c**, **4a**, and **4b** were collected with an Agilent SuperNova single-source diffractometer (Eos CCD detector) using mirror monochromatized Mo K α radiation (λ = 0.71073 Å) and CRYALISPRO⁴⁵ for data collection and reduction. The structures were solved by direct methods using SIR2014⁴⁶ and full-matrix, least-squares refinements on F^2 were performed using SHELXL-2018/3⁴⁷ programs. The reflections were corrected for Lorentz polarization, and multi-scan (SADABS⁴⁸) or analytical (CRYALISPRO⁴⁵) absorption correction was applied. More SCXRD details can be found in the [Supporting Information](#). The figures were drawn with Mercury.⁴⁹

2.3.4. Powder X-ray Diffraction. The PXRD patterns of **1–4** were measured using a Malvern Panalytical X'Pert PRO diffractometer with Cu K α radiation (λ = 1.54187 Å via Ni β -filter; 45 kV, 40 mA). Data processing and search-match phase analyses were carried out by program X'pert HighScore Plus v. 4.9 and ICDD-PDF4+ database (version 2020).^{50,51} More PXRD details can be found in the [Supporting Information](#).

2.3.5. Thermal Analysis. TG analyses were performed using a PerkinElmer STA 6000 thermogravimetric TG/DSC analyzer. Each sample was prepared in an open platinum crucible and was measured under an air atmosphere (flow rate of 40 mL/min), with a heating rate of 10 °C/min, in the temperature range of 22–600 °C. Thermal transitions of the products were also examined by a power compensation PerkinElmer 8500 series differential scanning calorimeter. All heating/cooling scans were carried out under a nitrogen atmosphere (flow rate 40 mL/min) using 50 μ L aluminum pans sealed by a 30 μ L aluminum pan with pinholes (resulting in 20 μ L of free volume for a sample).

2.4. Computational Methods. The geometries of molecular and ionic species were optimized in the gas phase using four different hybrid exchange–correlation functionals, namely, the PBE0,^{52,53} B3LYP,^{53–55} M06-2X,⁵⁶ and ω B97X,⁵⁷ in conjunction with def2-TZVP^{58,59} basis sets. The core electrons of iodine atoms were described using effective core potential.⁶⁰ The PBE0 and B3LYP optimizations were also carried out with dispersion correction using Grimme's dispersion correction (D3) with the Becke–Johnson damping function.^{61,62} For all studied systems, two different geometry optimizations were performed. In the first optimization, only the positions of hydrogen atoms were optimized, and the positions of other atoms were frozen to their crystal structure coordinates, whereas in the second optimization, no geometry constraints were used (full geometry optimization). All gas-phase calculations were carried out with Gaussian 16,⁶³ and the natural energy decomposition analyses were performed with the NBO 7.0 program.⁶⁴

Periodic boundary calculations for crystal structures of **1**, **1a**, **2e**, **2c**, and **3** were performed using the CRYSTAL17 program package,⁶⁵ employing the PBE0 hybrid functional combined with Grimme's D3 model to treat the dispersion interactions and pob-TZVP triple-zeta valence basis sets^{66,67} designed for solid-state calculations. k-points within the Brillouin zone of the reciprocal space were sampled according to the Monkhorst–Pack method applying a grid of 8 \times 8 \times 8. Default tolerance factors were used for evaluating the Coulomb and exchange integrals, and default SCF convergence and optimization thresholds were used in the optimizations.

To evaluate the influence of def2-TZVP and pob-TZVP basis sets, used in the gas-phase and solid-state calculations, respectively, on the results, gas-phase calculations for **1_{mon}**, **1a_{mon}**, and **2e_{mon}** were carried out at the PBE0-D3/def2-TZVP and PBE0-D3/pob-TZVP levels of theory. The basis set dependence of the gas-phase calculations was minimal (see below, [Figure 7](#)). Thus, def2-TZVP basis sets were used in all other gas-phase calculations.

To ensure that the basis set superposition error (BSSE) does not significantly affect the calculated interaction energies of the investigated compounds, the BSSE energies were calculated for **1_{mon}**, **1a_{mon}**, and **2e_{mon}** using the counterpoise correction method as implemented in Gaussian at the M06-2X/def2-TZVP level of theory.^{63,68,69} The calculated values for **1_{mon}**, **1a_{mon}**, and **2e_{mon}** were 1.69, 2.59, and 5.65 kJ/mol, respectively. If these BSSE energies are compared to the total interaction energies of the investigated compounds ([Table 2](#)), it can be concluded that the BSSE has only a minute effect, less than 1.6%, on the total interaction energies of the investigated compounds. Thus, no BSSE corrections were calculated for other systems.

3. RESULTS AND DISCUSSION

3.1. Synthesis. The synthesis of compound **1** performed in CH₃CN gave the product with good yield and purity, whereas the syntheses of **2** and **3** in CH₃CN did not lead to any isolated amount of the targeted main products. In the case of **2**, the poor conversion led to the formation of monocation **2e** and halogen-bonded 3IPy trapping complex **2d** (see below), which were not isolated, but their crystal structures were obtained (see below). Changing the solvent to DMF improved the conversion and yields of the products **2** and **3**. However, NMR studies showed the synthetic product **2** to contain 3IPy in an almost 1:2 (3IPy/2) ratio. A further PXRD study indicated product **2** to be a mixture of two phases (later identified as **2a** and **2d**, see the discussion below). The MS spectrum of **2** was consistent with the dication being the main cationic species in the product ([Figure S22](#)). Compared to the yield of *m*-isomer **2** (28%), the yield of *p*-isomer **3** (83%) is remarkably better, which could be the result of better conversion and more efficient product precipitation from DMF in the case of **3**. Because of the abovementioned observations with **2** and **3**, the synthesis of compound **4** was at first attempted in DMF without success. Instead, compound **4** was successfully synthesized in CH₃CN. NMR spectra of product **4** showed the two possible conformations of the trication, where three 3IPy⁺ units can either lie on the same side of the plane of the central benzene ring or one of them can lie on the opposite side.

3.2. Crystallographic Studies. In the present study, a total of 15 single crystal structures showing XB interactions were obtained. The normalized interaction ratio (R_{XB})²⁴ was calculated for all the observed halogen bonds ([Table 1](#)) to estimate the XB interaction strengths and simplify the comparison of XB distances between different structures with variable acceptors.

Two polymorphic crystal structures were obtained from **1** (*N*-ethyl-3IPy⁺I[−]). Crystals obtained from CH₃CN solution

Table 1. Normalized Interaction Ratios (R_{XB})²⁴ for Halogen Bonds Observed in the Crystal Structure Analyses of This Study

C–I⋯I [−] interactions		C–I⋯Br [−] interactions		C–I⋯O interactions	
structure	R_{XB} ^a	structure	R_{XB} ^a	structure	R_{XB} ^a
1	0.88	2a	0.86 ^b	1a	0.85
1′	0.89	2b	0.85	2c	0.86
1′	0.89	2b	0.86	3a	0.84
1b	0.89	2d	0.84 ^b	3a	0.87
1b	0.89	2d	0.85 ^b	3b	0.88 ^b
1c	0.89	2e	0.87	4b	0.91
1c	0.90	3	0.86 ^b		
4a	0.88 ^c	3	0.88 ^b		
		4a	0.90 ^d		
		4b	0.85		
		4b	0.87		

^aShortest interaction in the structure given first. ^bTwo or ^cthree equivalent interactions. ^dMinor component of disorder.

contained only one ion pair in the asymmetric unit (AU). This structure of **1** is crystallized in the same space group ($P2_1/n$) as a recently reported polymorphic structure but shows a different intermolecular geometry.³⁰ A second polymorph **1′** from EtOH solution was crystallized in the triclinic space group (P –

1) and showed two ion pairs in the AU (Figure 1). PXRD study of product **1** from synthesis gave a diffraction pattern that did not match either of the patterns simulated from SCXRD data of **1** or **1′** (Figures S40 and S41) but matches well with the phase reported by Fotović and Stilić.³⁰ The findings indicate that at least three polymorphic forms exist for compound **1**.

Anion metathesis reactions of **1** with silver triflate (AgOTf) and ammonium hexafluorophosphate in H₂O gave crystal structures **1a** and **1c**, respectively, while co-crystallization with 2,6-lutidine (2,6-dimethylpyridine) in CH₃CN resulted in **1b** (Figure 1). *N*-Ethyl-3IPy⁺OTf[−] (**1a**) showed only one ion pair in the AU, like **1**. Structure **1b** consists of one disordered 2,6-lutidinium and two *N*-ethyl-3IPy⁺ cations with three I[−] anions in the AU. Two *N*-ethyl-3IPy⁺ cations, one I[−], and two-halves of PF₆[−] were found in the AU of structure **1c**, meaning that the anion exchange was successful for one-half of I[−] present in **1**.

In all these structures, 3IPy⁺ units participate in XB interactions with similar geometries associating anions to cations (Table 1 and Figure 1). In **1**, every I[−] is bound by one C–I⋯I[−] interaction like in the literature structure,³⁰ while in **1′**, **1b**, and **1c**, one I[−] is bound with two C–I⋯I[−] contacts and the other iodide in the AU does not act as an XB acceptor. The C–I⋯I[−] interaction in **1** is only around 0.05 Å shorter than the ones in **1′**, **1b**, and **1c**, where I[−] is bound by two halogen

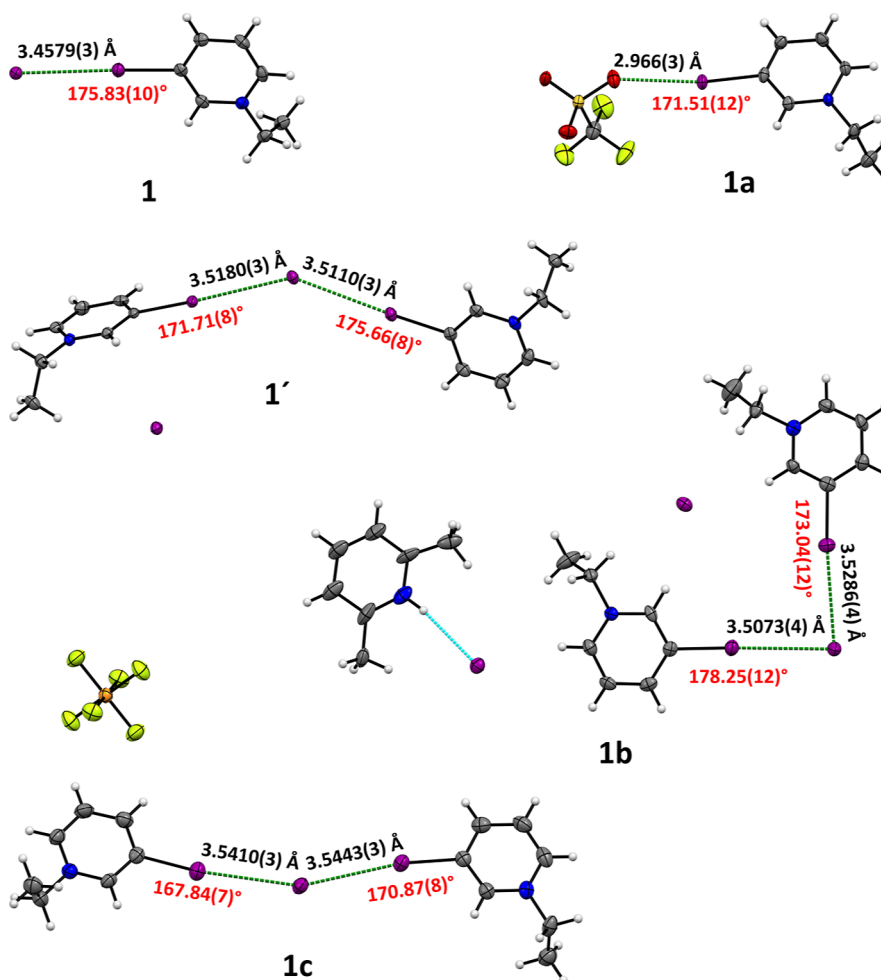


Figure 1. Crystal structures of **1**, **1′**, and **1a–1c** showing XB (green sticks), N–H⋯I[−] interaction (**1b**, cyan stick), I⋯A distances (black), and C–I⋯A angles (red). Disorder of the lutidinium cation (**1b**) and the alternative PF₆[−] position (**1c**) were removed for clarity.

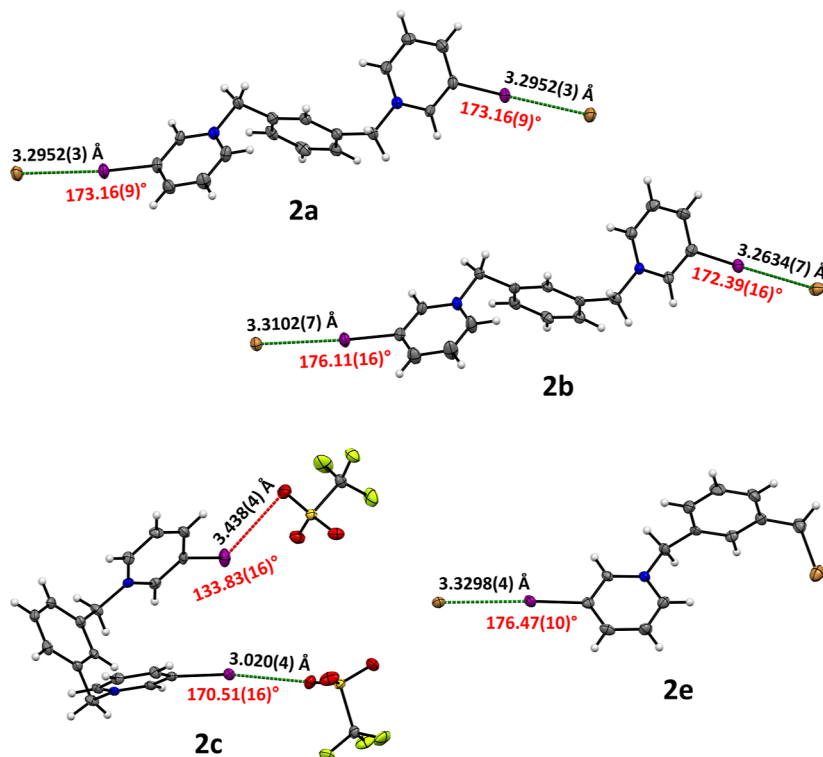


Figure 2. Crystal structures of 2a – 2c and 2e showing XB (green sticks), I...A distances (black), and C–I...A angles (red). H₂O molecules in 2a and 2b were removed for clarity. Non-XB C–I...O contact in 2c is shown with a red stick.

bonds. Geometries around anions accepting two halogen bonds in 1', 1b, and 1c are all different, showing I...I...I angles close to 146, 84, and 160°, respectively. The OTf[−] anion is connected to the cation in 1a by one associative C–I...O interaction, which has a shorter normalized distance (Table 1) than the C–I...I[−] interactions in the other four structures. This is expected due to the smaller size of the oxygen atom, resulting in higher strength of the XB interaction.²³ This geometrical examination indicates that the highly linear XB interactions in these *N*-ethyl-3IPy⁺ structures ($\angle_{\text{XB}} > 167^\circ$, Figure 1) have a significant role in the association of cations to anions despite the relative weakness of XB contacts, as indicated by the R_{XB} values of 0.90–0.88.

The ionic forces and XB interactions are assisted in anion binding by several other weak contacts in the crystalline state. These contacts for all investigated structures in this paper are visualized and discussed in the Supporting Information (Section 3.2 and Figures S25–S39). The influence of these competing weak interactions in the formation of different polymorphs of 1 can be presumed, but the data of 1 and 1' or the literature data³⁰ did not show any lucid support for it. The literature structure is showing the least number of weaker interactions, while they are more numerous and of similar quantity in 1 and 1'. Furthermore, I[−] and Br[−] anions in all structures reported in this study show varying numbers of weaker interactions regardless of whether they are halogen-bonded or not. In other words, the observed intermolecular forces do not directly explain the occurrence of polymorphism of compound 1.

Crystallization experiments with compound 2 resulted in, in total, five different crystal structures of 2. The AU of 2a obtained from D₂O is composed of a half of a dication, one Br[−] anion, and 1.25 H₂O molecules, and thus, the overall molecular

structure is 2₂·5H₂O. Crystallization from water also yielded a second structure 2b, wherein the AU consists of a dication, two Br[−] anions, and 2.75 H₂O molecules (2 · 2.75H₂O). An anion metathesis made in water using AgOTf resulted in a crystal structure of a non-hydrated dicationic ditriflate 2c (Figure 2). The experimental origin for the crystal structures 2d and 2e was the unresolved product mixture obtained from the initial reaction attempts carried out in CH₃CN. The presence of unreacted 3IPy molecules in the reaction mixture yielded the structure 2d, which was obtained by recrystallization from MeNO₂. In 2d, two dications are bridged by two Br[−] anions, forming a cavity that is assembled around a disordered 3IPy molecule (Figure 3). The other Br[−] anions are disordered over three positions, giving the overall structure of 2d as 2₂·(3IPy). A monocationic structure 2e was obtained when α,α' -

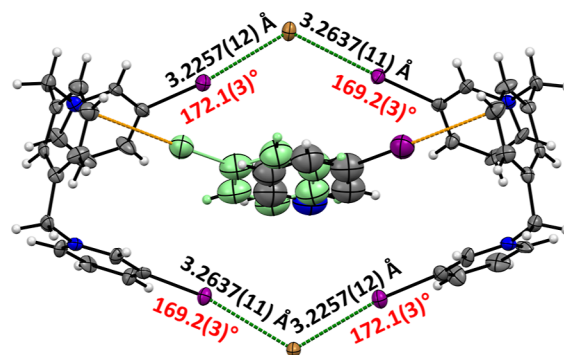


Figure 3. Crystal structure of complex 2d showing the disorder of 3IPy in the cavity as well as XB (green sticks), C–I... π contacts [orange sticks, $d_{\text{I} \cdots \pi} = 3.603(12)$ Å], I...Br[−] distances (black), and C–I...Br[−] angles (red). Two disordered bromides were removed for clarity.

dibromo-*m*-xylene reacted with only one molecule of 3IPy. The structure afforded by recrystallization from acetone consisted of a monocation with the bromomethyl group and Br[−] as a counter anion (Figure 2).

The 3IPy⁺ units in both **2a** and **2b** show similar C–I⋯Br[−] XB geometries in anion binding (Table 1 and Figure 2). In **2a**, these contacts are equal due to symmetry. One OTf[−] in **2c** is bound to the dication by a C–I⋯O halogen bond that is geometrically similar (Figure 2) to that observed in **1a**. The other OTf[−] shows a long and non-linear C–I⋯O contact to the other 3IPy⁺ unit of the dication (Figure 2), which is not considered to be an actual XB interaction. In **2e**, the cation and the anion are associated by C–I⋯Br[−] interaction (Figure 2), but the bromine in the bromomethyl group does not participate in any XB interactions.

In **2d** (Figure 3), the cavity that is trapping a neutral 3IPy molecule exhibits four C–I⋯Br[−] interactions between dications and anions. The geometries of C–I⋯Br[−] interactions are similar to the ones observed in **2a** and **2b** (Table 1). The 3IPy molecule inside the cavity is disordered around the fourfold inversion axis by a 180° turn in such a way that the 3-iodo substituent in both orientations is pointing toward a benzene ring of one of the dications. Thus, the complex is further strengthened by the resulting weak C–I⋯ π contact. The shortest I⋯C distances are similar to that of the anion⋯ π contacts observed in structures **1**, **1'**, **1b**, and **1c** (see Supporting Information, Section 3.2).

The Pawley fit of the PXRD pattern measured for the synthetic product **2** from DMF (see above) matched well to that of the unit cell parameters of **2d** obtained by SCXRD (Figure S42). The PXRD analysis showed also that the synthetic product contained small amounts of structure **2a**. These findings are consistent with the ¹H NMR spectrum of the synthetic product, which indicated the presence of unreacted 3IPy in an almost 1:2 (3IPy/2) ratio and explains why the integrals of 3IPy were slightly smaller (roughly 0.8:2). The attempted washing of the solid product **2** to remove extra 3IPy by refluxing it in CHCl₃ failed. We postulate that the failure to remove 3IPy from the product is due to the strong binding of 3IPy in complex **2d**, thus making its removal significantly unfavorable.

Compound **3** was crystallized from water. The AU of structure **3** is composed of two Br[−] anions and two halves of a dication. The molecular 3D structures of these dications are divergent with deviating dihedral angles. Due to symmetry, both ends of both dications show equal C–I⋯Br[−] interactions involving anions labeled as Br2 in Figure 4. These two separate XB contacts connect dications and Br2 anions into infinite chains throughout the crystal, and their interaction geometries are similar to those found for structures derived from **2** (Table 1 and Figures 2, 3, and 4). The only significant differences are I⋯Br⋯I angles for Br[−] anions accepting two halogen bonds that are much more linear in **3** (165°) than in **2d** (113°). The experimental PXRD pattern of product **3** fits well with the simulated one from SCXRD data of **3**, except for few extra unindexed peaks that indicate the presence of another unknown crystalline phase (Figure S43).

The anion metathesis experiment for **3** with AgOTf yielded two unexpected crystal structures from water (**3a**) and aqueous DMF (**3b**) solutions. Structure **3a** has one dication, six Ag⁺ cations, eight triflates, and one H₂O molecule in the AU. The triflates are connected to Ag⁺ cations by coordinative Ag–O bonds forming a polymeric AgOTf architecture that is assisted

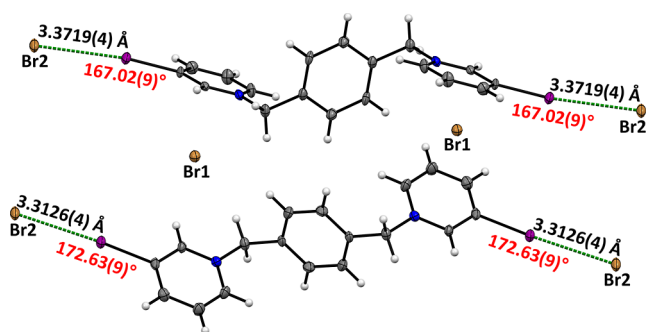


Figure 4. Crystal structure of **3** showing XB (green sticks), I⋯Br[−] distances (black), C–I⋯Br[−] angles (red), and Br[−] labeling. Bromides (Br2) on the left belong to the next AU.

by H₂O molecules, which are coordinated to two Ag centers. The dications are associated to adjacent AgOTf polymers through C–I⋯O interactions formed (Figure 5). One of the

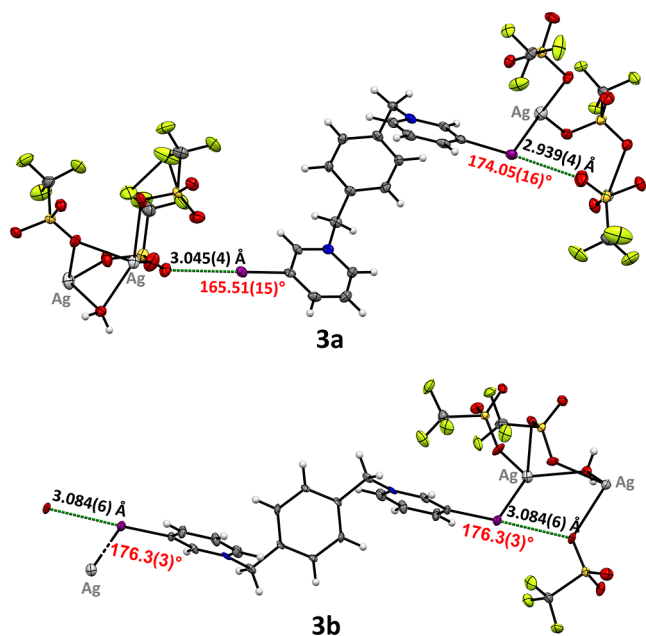


Figure 5. Parts of the crystal structures of **3a** and **3b** showing XB (green sticks), I⋯O distances (black), and C–I⋯O angles (red). Silver atoms are also labeled (gray).

XB interactions is supported by the Ag–I coordination bond. This deviates from **2c**, where only one iodine of the *m*-dication participated in XB. A related polymeric system is observed in **3b**, where the AU is composed of a half of a dication, 11 Ag⁺, 12 triflates, a DMF, and a H₂O molecule. The solvent molecules (H₂O and DMF) are included in the AgOTf polymer structure. The dication is again located between these polymeric systems, and both ends are connected to polymer by symmetry-related Ag–I and C–I⋯O bonds (Figure 5).

Of the C–I⋯O interactions in **3a**, the one supported by Ag–I is more than 0.1 Å shorter ($R_{\text{XB}} = 0.84$) than the free halogen bond ($R_{\text{XB}} = 0.87$, Figure 5 and Table 1). On the other hand, the Ag–I-supported halogen bond in **3b** is 0.15 Å longer than the corresponding contact in **3a**. One could think that the geometrical difference of these interactions with coincident Ag–I bonds originates from the divergence in C–I–Ag⁺ angles, which are closer to orthogonal in **3b** (96°, cf. 107° in

3a), thus making the Ag–I bond oriented closer to the halogen bond acceptor (O-atom) in 3a. This makes the Ag–I and halogen bonds in 3a more unidirectional, which could result in enhanced cooperativity of the bonds as the shorter halogen bond than that of 3b would indicate. However, investigation of the few loosely related structures found from the CSD³⁸ does not support this explanation as clear trends involving the influence of the C–I–Ag⁺ angle or I–Ag⁺ distance on XB were not observed.^{70–72} Overall, the C–I⋯O geometries in all triflate structures 1a, 2c, 3a, and 3b are rather similar with close to linear contact angles and equal R_{XB} values (Table 1), also matching well the parameters reported by Kniep et al.⁷³ for a related triflate structure [(N-Me-3IPy-4-yl)₂N₂][OTf₂].

Our crystallization tests with compound 4 did not give a phase pure product, but instead, two different crystalline phases (4a and 4b) were obtained. The crystallization by slow evaporation of formamide solution gave crystal 4a, structurally determined as (C₂₇H₂₇I₃N₃)Br₂I salt. When crystallized from MeOH solution, the solvated structure 4b was obtained, which contained 2.5 MeOH molecules. The structures are distinguished by four main features: (1) all 3IPy⁺ units of the trication lie on the same side of the plane of the central benzene ring; (2) covalently bound iodine atoms are pointing to the side, and trication shows a three-fold symmetry; (3) both structures show a cavity wherein the halide ion is bound on the top of the central benzene ring and located between pyridinium units; and (4) all 3IPy⁺ units in both structures act as halogen bond donors. One recent literature structure, the MeCN solvate of 1,3,5-tris((3IPy⁺)methyl)-2,4,6-tris(*n*-hexyloxy)benzene triiodide, was found to show similar features, except that its cavity is filled with a CH₃CN molecule instead of a halide.²⁸ In 4b, the three-fold symmetry of the structure is suppressed by a MeOH molecule, which accepts a halogen bond donated by one of the iodines. The cavity halide position in the crystal data of 4a is so rich with electron density that it is unlikely to be occupied by a mere Br[−] anion, but instead, it is disordered, showing shared occupancy between I[−] and Br[−] anions with an around 3:1 (I[−]/Br[−]) ratio. The source of the I[−] and its appearance instead of Br[−] in the structure are due to the decomposition of 3IPy units during the crystallization, as described previously for halopyridines.^{74,75} The halide in the cavity accepts three weak C–H⋯I[−] (4a) or C–H⋯Br[−] (4a and 4b) hydrogen bonds from the trication (Figure 6). The PXRD study of the synthetic product 4 showed it to be weakly crystalline, and surprisingly, the pattern seems to match better with methanol solvate 4b (Figure S44).

All three halogen bonds in 4a show equal XB parameters (Table 1 and Figure 6) due to high three-fold symmetry. These C–I⋯I[−] interactions connect the trication to I[−] in the cavity of three adjacent AUs and every I[−] accepts three halogen bonds. All XB interactions in 4b show high linearity. Two of them are accepted by the Br[−] in the cavity of the adjacent AUs and the third by the MeOH oxygen atom. The C–I⋯Br[−] bonds involving Br[−] in the cavity show similar geometries (Table 1 and Figure 6) to all the other XB interactions accepted by Br[−] in the present study. The third halogen bond that was accepted by a halide in the cavity of 4a is substituted in 4b by additional C–H⋯Br[−] contacts from a third adjacent trication (Figure S39). The halogen bond accepted by MeOH appears to give a C–I⋯O geometry with a longer I⋯O distance (Table 1) than the same interaction in triflates 1a, 2c, 3a, and 3b or nitrate,³⁷ which deviates from the previous findings between the 1,3,5-tris((3IPy⁺)methyl)-2,4,6-tris(*n*-hexyloxy)benzene trication

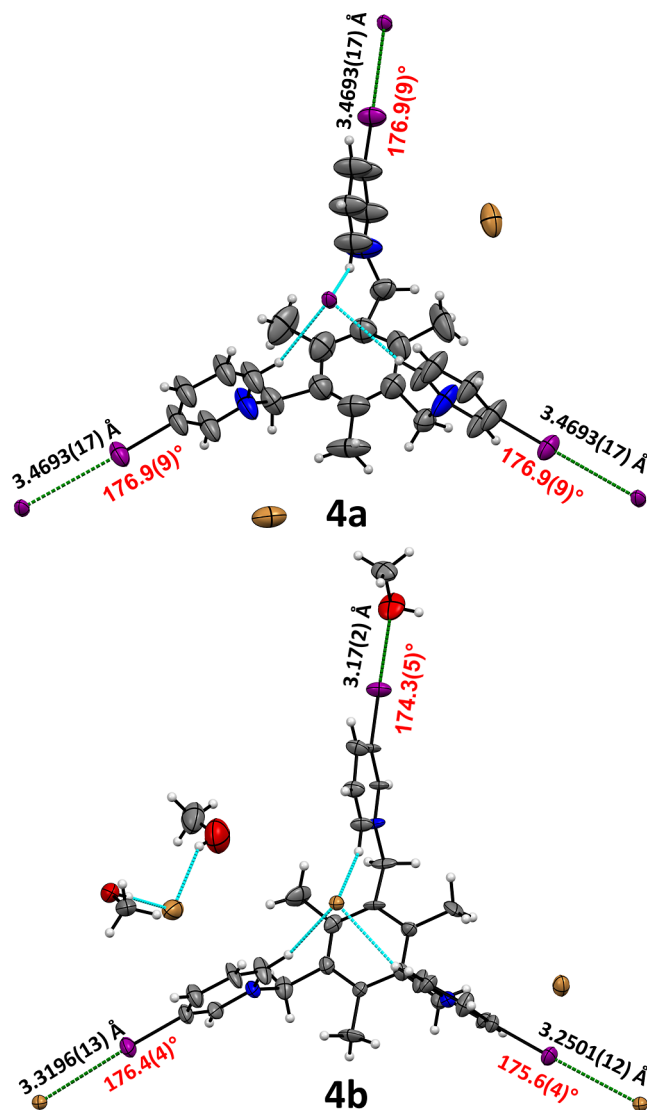


Figure 6. Crystal structures of 4a and 4b showing the XB (green sticks), hydrogen bonds (cyan sticks), I⋯A distances (black), and C–I⋯A angles (red). Only one component of the disordered structures is shown for clarity. The halogen-bonded I[−] and Br[−] anions belong to the next AU.

and MeOH.²⁸ It should be noted that in 4b, the surroundings of the halogen-bonded MeOH are somewhat disordered, and the hydroxyl group donates a hydrogen bond to another half-populated MeOH molecule, potentially inducing the lengthening of the C–I⋯O interaction.

The observed XB interactions in all *N*-alkyl-3IPy⁺ salts presented here show geometric values in the same range as the ones found from the literature. All C–I⋯A angles are close to linear (>165°), and, for example, the lowest observed angle of 165.5° in 3a (C–I⋯O, Figure 5) corresponds well with most angles reported for halogen bonds between the *N*-methyl-3IPy⁺ moiety and triflate by Berryman and co-workers.⁷⁶ The found I⋯I[−] interaction distances have an average R_{XB} value of 0.89 (Table 1), which is slightly longer than the one (R_{XB} = 0.88) calculated from the literature geometries of the *N*-alkyl-3IPy⁺ moiety containing iodides.^{28,30,32,34,37,77–79} The shortest reported I⋯I[−] halogen bond donated by the *N*-alkyl-3IPy⁺ moiety in the literature is 0.15 Å shorter than the shortest one of this study in 1 (Figure 1).⁷⁷ The observed I⋯Br[−] halogen

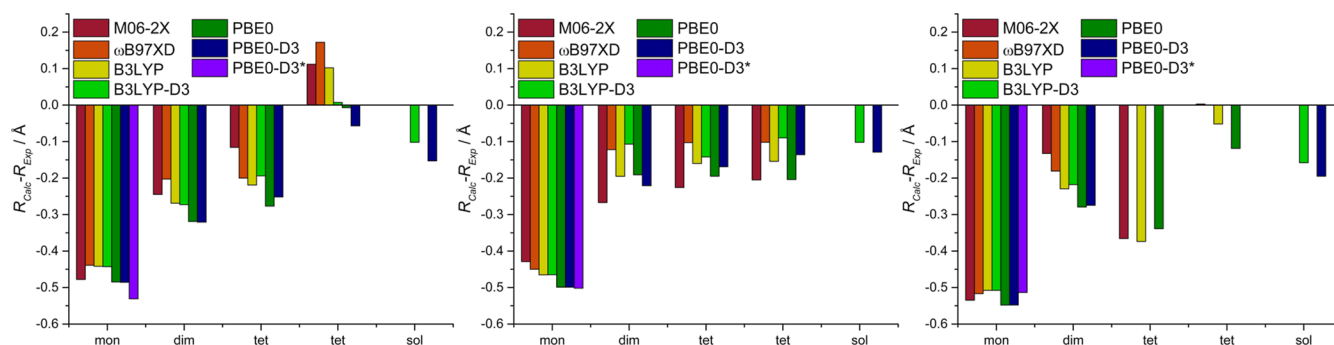


Figure 7. Difference in length between experimental and optimized halogen bonds for **1** (left), **1a** (middle), and **2e** (right). Two different values are given for tetramers as they contain two halogen bonds with different lengths. Values for the **2e_{tet}** tetramer at the PBE0-D3, B3LYP-D3, and ω B97XD levels are omitted from the figure because their gas-phase optimized geometries did not converge to the correct minimum. PBE0-D3* denotes the results obtained with the pob-TZVP basis set, and all other gas-phase results are obtained with the def2-TZVP basis set. mon = monomer, dim = dimer, tet = tetramer, and sol = solid.

bond distances in average are well in line with average distances ($R_{XB} = 0.86$) for *N*-alkyl-3IPy⁺ moieties found from the literature.^{28,30,32,34,37,73,77,80} The shortest I⋯Br[−] is observed in complex **2d**, which is still 0.1 Å longer than the shortest one reported by Berryman and co-workers.⁷⁷ Only the observed I⋯O halogen bond distances in **1a** and **3a** are shorter than 3 Å, which are among the distances for most I⋯O halogen bonds in *N*-alkyl-3IPy⁺ triflate structures in the literature.^{28,34,73,76,81} However, despite their relative weakness, the XB interactions observed in the present study show their importance in anion binding and in packing of the structures and, furthermore, sustain their directionality even better than in most other reported systems.

In addition to a simple 1:1 binding between the *N*-alkyl-3IPy⁺ unit and the monoatomic anion or oxygen atom of triflate, observed in **1**, **1a**, **2a–c**, and **2e**, the binding of an anion by two (**1'**, **1b**, **1c**, **2d**, **3**, and **4b**) or three (**4a**) simultaneous halogen bonds from *N*-alkyl-3IPy⁺ units was observed. Similar anion binding by two *N*-alkyl-3IPy⁺ units was found from a few literature reports with comparable XB geometries, which occurred either by the dication having two 3IPy⁺ units as bidentate binding^{34,81} or by 3IPy⁺ units of separate cations.^{28,37,73,78} Our literature search did not give any related structure to **4a** with three simultaneous halogen bonds, although one literature structure showed four halogen bonds accepted by Cl[−].⁸¹ In that sense, and with high symmetry, the reported structure of **4a** has a certain uniqueness.

3.3. Thermal Analysis. Based on TG/DSC analyses, the extrapolated initial temperatures of thermal decomposition of products **1** to **4** ranged from 165 to 203 °C, with the lowest temperature being 165 °C for **2** and the highest being 203 °C for **1** (see Figure S45 and Table S5 in the [Supporting Information](#)). The observed onset values are similar to that of *N*-alkyl-3-halogenopyridinium salts previously reported by Fotović et al.^{30–32} The first major step in the thermal decomposition process is relatively rapid, and by about 300 °C, weight losses in all four products typically ranged from 68 to 99 wt.-%, thus indicating complete decomposition of the compounds. As an exception to other products, for **2**, a minor distinctive weight change of ~7 wt % from (143–190 °C) is seen prior to the major decomposition step (see further details in the [Supporting Information](#)). The last slowly decreasing weight loss up to a final temperature of 600 °C corresponds to the slow evaporation of carbonaceous decomposition products through various pyrolysis and combustion reactions, which can

be seen as endothermic and exothermic changes on the DSC curve in the corresponding temperature range. Of the compounds analyzed, only compound **1** showed a melting point (135.6 °C; observed also by a melting point apparatus) before the initial temperature of thermal decomposition. Further details of the TG/DSC analyses and the DSC analyses of the products are described in the [Supporting Information](#).

3.4. Computational Studies. Even though the XB is often utilized in the crystal engineering in the solid state, most of the previous computational studies focusing on XB systems have been carried out in the gas phase and only a small number of studies have included solid-state calculations.^{82–88} Gas-phase calculations offer an excellent procedure to study the strength and nature of the XB in a single halogen-bonded unit consisting of a halogen bond donor and a halogen bond acceptor. Unfortunately, the gas-phase calculations for single halogen-bonded units easily exaggerate the role of halogen bonds in the solid-state packing of an investigated system because most of the other crystal packing effects are excluded from these calculations. The poor performance of gas-phase calculations is particularly emphasized in systems where strong electrostatic interaction between a negatively charged halogen bond acceptor and a positively charged halogen bond donor dominates the total interaction energy over other intermolecular interactions like in the systems studied here (see below). However, there are potential ways to overcome the above shortcomings. The size of the model system can be increased to account for additional interactions, or calculations can be carried out using periodic boundary conditions modeling the whole solid-state material. To investigate the effectiveness of these strategies for charged systems and to further study the role of halogen bonds and other intermolecular interactions in the solid-state packing of the investigated compounds, we carried out DFT calculations for selected model systems both in the gas phase (**1_{mon}**, **1_{dim}**, **1_{tet}**, **1a_{mon}**, **1a_{dim}**, **1a_{tet}**, **2e_{mon}**, **2e_{dim}**, **2e_{tet}**, **3IPy** + Br₂, **3IPy** + I₂, and **3IPy** + CF₃SO₃H; mon = monomer, dim = dimer, and tet = tetramer) and in the solid state (**1**, **1a**, **2c**, **2e**, and **3**). Previous studies have shown that the DFT methods can describe the complicated nature of the XB, arising from the electrostatic, dispersion, polarization, and charge transfer effects, accurately enough.⁸⁹ To assess the performance of different hybrid exchange–correlation functionals in describing the XBs, we used four functionals in the gas-phase calculations, namely, PBE0-(D3),^{52,53} B3LYP-(D3),^{53–55} M06-2X,⁵⁶ and

Table 2. Calculated Interaction Energies^a (ΔE , kJ mol⁻¹) per Each XB Unit for the Fully (F) and Only Hydrogen Positions (H) Optimized Gas-Phase Structures of **1**, **1a**, and **2e** as Well as the Percentage Ratios between ΔE_{mon} and ΔE_{dim} (%-mon/dim) and between ΔE_{mon} and ΔE_{tet} (%-mon/tet)

1	$\Delta E_{\text{mon}}(\text{F})$	$\Delta E_{\text{mon}}(\text{H})$	$\Delta E_{\text{dim}}(\text{F})$	$\Delta E_{\text{dim}}(\text{H})$	%-mon/dim(F)	%-mon/dim(H)	$\Delta E_{\text{tet}}(\text{F})$	$\Delta E_{\text{tet}}(\text{H})$	%-mon/tet (F)	%-mon/tet (H)
PBE0	-333.4	^b	-384.8	^b	86.6	^b	-430.7	^b	77.4	^b
PBE0-D3	-338.7	-310.2	-401.1	-389.9	84.4	79.6	-468.5	-422.6	72.3	73.4
B3LYP	-326.1	^b	-371.2	^b	87.8	^b	-410.1	^b	79.5	^b
B3LYP-D3	-336.6	-310.8	-399.2	-388.7	84.3	80.0	-470.2	-423.3	71.6	73.4
M06-2X	-318.9	-293.3	-382.8	-375.8	83.3	78.1	-452.7	-406.0	70.4	72.3
ω B97XD	-310.7	-289.7	-377.1	-372.2	82.4	77.8	-429.8	-405.0	72.3	71.5
1a	$\Delta E_{\text{mon}}(\text{F})$	$\Delta E_{\text{mon}}(\text{H})$	$\Delta E_{\text{dim}}(\text{F})$	$\Delta E_{\text{dim}}(\text{H})$	%-mon/dim(F)	%-mon/dim(H)	$\Delta E_{\text{tet}}(\text{F})$	$\Delta E_{\text{tet}}(\text{H})$	%-mon/tet (F)	%-mon/tet (H)
PBE0	-277.5	^b	-369.8	^b	75.0	^b	-392.4	^b	70.7	^b
PBE0-D3	-286.8	-244.2	-404.3	-326.8	71.0	74.7	-418.1	-373.9	68.6	65.3
B3LYP	-269.6	^b	-364.4	^b	74.0	^b	-380.3	^b	70.9	^b
B3LYP-D3	-286.1	-246.5	-400.7	-330.6	71.4	74.6	-421.6	-377.7	67.9	65.3
M06-2X	-275.6	-238.5	-347.2	-320.2	79.4	74.5	-385.9	-364.9	71.4	65.4
ω B97XD	-274.4	-239.1	-388.4	-323.7	70.7	73.9	-411.8	-370.1	66.6	64.6
2e	$\Delta E_{\text{mon}}(\text{F})$	$\Delta E_{\text{mon}}(\text{H})$	$\Delta E_{\text{dim}}(\text{F})$	$\Delta E_{\text{dim}}(\text{H})$	%-mon/dim(F)	%-mon/dim(H)	$\Delta E_{\text{tet}}(\text{F})$	$\Delta E_{\text{tet}}(\text{H})$	%-mon/tet (F)	%-mon/tet (H)
PBE0	-352.2	^b	-436.1	^b	80.8	^b	-585.1	^b	60.2	^b
PBE0-D3	-356.1	-319.2	-455.0	-438.6	78.3	72.8	^c	^c	^b	^c
B3LYP	-345.5	^b	-421.8	^b	81.9	^b	-678.5	^b	50.9	^b
B3LYP-D3	-353.3	-320.1	-453.6	-436.8	77.9	73.3	^c	^c	^c	^c
M06-2X	-338.2	-305.1	-442.6	-426.5	76.4	71.5	-440.5	-431.3	76.8	70.7
ω B97XD	-332.1	-302.2	-435.6	-424.7	76.2	71.2	^c	^c	^c	^c

^aInteraction energies were calculated using following equations: $\Delta E_{\text{mon}} = E_{\text{mon}} - [E(\text{cation}) + E(\text{anion})]$, $\Delta E_{\text{dim}} = [E_{\text{dim}} - \{2 \times E(\text{cation}) + 2 \times E(\text{anion})\}]/2$, and $\Delta E_{\text{tet}} = [E_{\text{tet}} - \{4 \times E(\text{cation}) + 4 \times E(\text{anion})\}]/4$. ^bNot calculated because for geometries where the positions of heavy atoms are kept frozen, the calculations with and without dispersion corrections will lead to similar interaction energies. ^cNot optimized to the correct local minimum.

ω B97XD,⁵⁷ out of which the latter two have been reported to describe the XB very well in other systems. Although other studies have shown that the inclusion of Grimme's dispersion correction (D3)^{61,62} into DFT calculations decrease the accuracy of the PBE0 and B3LYP hybrid functionals in describing the XB, the performance of these two functionals was tested with and without the dispersion correction in this study. The inclusion of D3 correction was considered because the crystal structures of **1**, **1a**, **2c**, **2e**, and **3** also contain other intermolecular interactions, such as weak hydrogen bonds and dispersion interactions, that are not properly described in the standard implementation of the B3LYP and PBE0. In the solid-state calculations, we utilized the PBE0-D3 and B3LYP-D3 exchange–correlation functionals.

Figure 7 shows the differences in the lengths of experimental and gas-phase optimized halogen bonds for **1**_{mon}, **1**_{dim}, **1**_{tet}, **1a**_{mon}, **1a**_{dim}, **1a**_{tet}, **2e**_{mon}, **2e**_{dim}, and **2e**_{tet}. The corresponding optimized structures from the gas-phase and solid-state calculations are given in Figures S47 and S48, respectively. It is evident from the calculated data that regardless of the choice of the hybrid exchange–correlation functional or basis set, the lengths of halogen bonds are heavily underestimated in the gas-phase optimized monomers because the halogen bonds in **1**_{mon}, **1a**_{mon}, and **2e**_{mon} are 0.43–0.55 Å shorter than the corresponding bonds in the crystal structures. The effect of different basis sets on the shortening of XBs is minimal, as revealed by the comparison of PBE0-D3/def2-TZVP and PBE0-D3/pob-TZVP results. The description of halogen bonds is improved when the gas-phase calculations are carried out for dimers **1**_{dim}, **1a**_{dim}, and **2e**_{dim}, but depending on the used functionals, the optimized halogen bonds are still 0.20–0.32, 0.11–0.26, and 0.13–0.27 Å shorter than the experimental ones for **1**, **1a**, and **2e**, respectively. Overall, the

M06-2X and ω B97XD functionals perform well for dimers, except the M06-2X for **1a**_{dim}. The PBE0 functional without and with the dispersion correction yields the shortest optimized halogen bonds for **1**_{dim} and **2e**_{dim}, indicating its poorer performance in the gas phase compared to that of other functionals. The dispersion correction has only a minimal influence on the optimized geometries of monomers and dimers, as shown by the PBE0-(D3) and B3LYP-(D3) calculations.

The description of XB is improved further by using tetramers as the model systems since each utilized functional predicts longer halogen bonds for tetramers than for monomers and dimers in the gas phase. At the M06-2X, PBE0-(D3) and B3LYP-(D3) levels of theory, some of the optimized halogen bonds in tetramers deviate less than 0.1 Å from the experimental results. This observation suggests that the size of the model system plays a larger role in the description of the XB in the gas phase than the choice of the functional if electrostatic interactions dominate the crystal packing of the investigated systems. Only the B3LYP-D3 method predicts one of the **1a**_{tet} halogen bonds to be a slightly shorter than that in **1a**_{dim} (<0.1 Å), and the outermost C–I⋯Br interactions in **2e**_{tet} are described to be shorter than those in **2e**_{dim} by all tested functionals. Furthermore, in the case of **2e**_{tet}, the PBE0-D3, B3LYP-D3, and ω B97XD functionals described the structure so poorly that they did not converge to the same local minimum as that for the M06-2X, PBE0, and B3LYP. The problem most likely originates from the large partial negative charge of the Br⁻ anion that leads to the overestimation of the electrostatic interaction between the cation–anion pair in the gas phase. Indeed, the natural energy decomposition analysis carried out for **1**_{mon}, **1a**_{mon}, and **2e**_{mon} at the M06-2X level of

theory shows that the electrostatic component dominates the total interaction energy of **2e_{mon}** (Table S7).

Although the gas-phase calculations describe the lengths of the halogen bonds in tetramers reasonably well, there are still some shortcomings in the gas-phase calculations, as mentioned above. The best agreement with the calculated and experimental structures is achieved when all plausible crystal packing interactions are included in the calculations through the solid-state calculations. To this end, the solid-state calculations at the PBE0-D3 level of theory produce reasonably well the experimental XB distances for **1**, **1a**, and **2e** as their calculated XB lengths differ 0.15, 0.13, and 0.20 Å from the experimental ones, respectively. Although the gas-phase calculations give a slightly better match for some of the halogen bonds than solid-state calculations, it should be noted that the performance of the solid-state calculations is robust and even the most problematic system (**2e**) is described correctly. To further prove the robustness of solid-state calculations, we also optimized two larger structures, **2c** and **3**, in the gas phase and solid state. As evident from the comparison in Figure S48, the geometries of **2c** and **3** are well described by the solid-state calculations, but the gas-phase calculations fail drastically.

To evaluate the strength of interaction energies in the studied systems, we carried out energy analyses for the gas-phase and solid-state optimized structures as well as for the model systems in which only the positions of hydrogen atoms were optimized while all other atoms were frozen to their crystal structure coordinates. The latter systems were considered because the geometries of gas-phase optimized structures of **1_{mon}**, **1_{dim}**, **1_{tet}**, **1a_{mon}**, **1a_{dim}**, **1a_{tet}**, **2e_{mon}**, **2e_{dim}**, and **2e_{tet}** deviated significantly from the solid-state structures, which further affects the interactions energies of the systems although the potential energy hypersurface along the halogen bond is usually relatively flat.^{89,90} The calculated interaction energies are listed in Table 2. It can be seen from the calculated interaction energies of monomers that the energy associated with the XB is very large. For example, the interaction energies calculated for the fully optimized **1_{mon}**, **1a_{mon}**, and **2e_{mon}** are −318.9, −275.6, and −338.2 kJ mol^{−1}, respectively, at the M06-2X level of theory, whereas the same energies for structures with only hydrogen positions optimized are 25.6, 37.1, and 33.1 kJ mol^{−1} weaker, respectively. All other functionals show a similar trend.

To investigate the effect the charges on the XB donors and acceptors have on the XB strengths, we optimized the geometries of XB systems consisting of neutral 3-iodopyridine donors and I₂, Br₂, or CF₃SO₃H acceptors for comparison. Depending on the halogen bond acceptor, the neutral systems have much longer halogen bonds, ranging from ~3.2 Å to 3.6 Å, as well as considerably smaller interaction energies that vary from −8.8 to −26.2 kJ mol^{−1} (Table S8). Two main conclusions can be drawn from the findings. First, the large interaction energies associated with the halogen bonds of **1_{mon}**, **1a_{mon}**, and **2e_{mon}** arise mostly from the favorable electrostatic interactions between the halogen bond donors and acceptors because the interaction energies of their charge balanced analogues are an order of magnitude smaller. Second, by comparing the interaction energies between the fully optimized monomers and those with only hydrogen positions optimized, it can be concluded that 12–16% contraction in the length of the halogen bond leads to 7–17% higher interaction energies. This result indicates clearly that gas-phase calculations carried

out for the optimized structures not only predict too short halogen bonds but also overestimate the strengths of halogen bonds between ions.

Compared to monomers, dimers and tetramers recover more “lattice energy” per halogen-bonded unit because they take into account all intermolecular interactions acting between anionic and cationic, anionic and anionic, and cationic and cationic units of which the dimer and tetramers consist of. Because of this, the contribution of halogen bonds to the total lattice interaction energy can be evaluated by taking the ratio of energies of the monomer and dimer or the monomer and tetramer. Depending on the employed functional and system, the percentage values for monomer–dimer ratios range from 70.7 to 84.4%, whereas monomer–tetramer ratios are from 50.9 to 76.2% for fully optimized geometries. Similar percentages are obtained if the ratios are taken from the interaction energies of the structures with only hydrogen positions optimized. The obtained ratios indicate that the calculated contributions of halogen bonds to the solid-state packing of **1**, **1a**, and **2e** become smaller when more realistic structures are used in the calculations. To evaluate the relative contribution of halogen bonds to the total lattice interactions, we determined the sum $\Delta E_{\text{total}} = \Delta E_{\text{lattice}} + \Delta E_{\text{int_XB}}$ for **1**, **1a**, and **2e**, in which ΔE_{total} , $\Delta E_{\text{lattice}}$, and $\Delta E_{\text{int_XB}}$ are the total interaction energy, interaction energy of the monomer with the rest of the crystal lattice derived from solid-state calculation, and interaction energy of the XB donor and acceptor within the monomeric unit calculated in the gas phase, respectively (Tables S9 and S10). Regardless of the used functional, the ratios of the $\Delta E_{\text{int_XB}}$ energies to ΔE_{total} for **1**, **1a**, and **2e** are 46, 39, and 41%, respectively, indicating that the XB contribution to the total interaction energies of **1**, **1a**, and **2e** is significant but less than 50%. However, without the strongly stabilizing electrostatic interaction, arising from the negatively charged halogen bond acceptor and positively charged halogen bond donor units, other intermolecular interactions would dominate the solid-state packing of the investigated systems, as exemplified above by the gas-phase calculation carried out for the charge neutral model systems.

4. CONCLUSIONS

The present study provides further evidence that cationic 3-iodopyridinium (3IPy⁺) moieties are effective halogen bond donors. Although the directional XB was found to be a secondary intermolecular interaction in all the 15 investigated crystalline complexes, it still showed significant effects on the arrangement of the ionic species, along with the solvent molecules, in the crystal lattice. Anion binding by XB donated by 3IPy⁺ was observed in crystal structures obtained from both organic and aqueous solutions. The strengths of these XB interactions were evidenced by a complex where a pair of two 3IPy⁺ moieties containing dications and two Br[−] anions formed a cavity by C–I⋯Br[−] interactions. The cavity was occupied by a neutral 3IPy molecule, and the formed complex was so stable that 3IPy could not be liberated from the solid even in boiling CHCl₃. The ability of the 3IPy⁺ moieties to bind neutral MeOH molecules by C–I⋯O interactions was demonstrated in the study. Furthermore, two complexes showed that the iodine atom of 3IPy⁺ unit is able to exhibit simultaneously C–I⋯O interaction and a coordination bond to Ag⁺, indicating that halogen bonds from 3IPy⁺ can sustain their high directionality even if competing interatomic forces are present.

The investigated crystal structures showed a rather versatile network of weak interactions, which are important for the stability and the strength of the complexes. DFT calculations carried out for the gas-phase and solid-state optimized structures resulted in three main observations. First, for charged systems in the gas phase, the size of the model system plays a larger role in describing XB correctly than the choice of utilized functionals. Second, in the relative strength order of intermolecular interactions, XB interactions come second to electrostatic interactions that are the main interaction between charged species. Third, even though the halogen bonds are weaker than electrostatic interactions, the directionality of XBs cause them to have a significant influence in determining the solid-state structures. Overall, not only do the results of the study increase the knowledge and understanding about XB involving weaker donors in the presence of strong electrostatic forces and other noncovalent interactions but they also show that the investigated 3IPy⁺ moiety can be utilized in the future, e.g., in selective anion sensing and capture and as well as a practical XB tool for crystal engineering in both organic and aqueous media.

■ ASSOCIATED CONTENT

SI Supporting Information

The Supporting Information is available free of charge at <https://pubs.acs.org/doi/10.1021/acs.cgd.2c01351>.

NMR and MS spectra of 1–4; additional crystallographic data refinement details, crystal data, and noncovalent intermolecular interaction schemes of SCXRD structures; experimental PXRD patterns and Pawley refined profiles (from SCXRD structures) of 1–4; TG curves of 1–4 and DSC curves of 1 with thermal analysis results; and additional computational results and xyz-coordinates (PDF)

Accession Codes

CCDC 2171079–2171093 contain the supplementary crystallographic data for this paper. These data can be obtained free of charge via www.ccdc.cam.ac.uk/data_request/cif, or by emailing data_request@ccdc.cam.ac.uk, or by contacting The Cambridge Crystallographic Data Centre, 12 Union Road, Cambridge CB2 1EZ, UK; fax: +44 1223 336033.

■ AUTHOR INFORMATION

Corresponding Authors

Jani O. Moilanen – Department of Chemistry, Nanoscience Centre, University of Jyväskylä, Jyväskylä 40014, Finland; orcid.org/0000-0002-2096-593X; Email: jani.o.moilanen@jyu.fi

Arto Valkonen – Department of Chemistry, University of Jyväskylä, Jyväskylä 40014, Finland; orcid.org/0000-0003-2806-3807; Email: arto.m.valkonen@jyu.fi

Authors

J. Mikko Rautiainen – Department of Chemistry, University of Jyväskylä, Jyväskylä 40014, Finland; orcid.org/0000-0002-3695-4151

Maryna Green – Department of Chemistry, University of Jyväskylä, Jyväskylä 40014, Finland; Present Address: Institute of Biotechnology, Helsinki Institute of Life Science (HiLIFE), Viikinkaari 1, 00014 University of Helsinki, Finland

Minna Mähönen – Department of Chemistry and Department of Chemistry, Nanoscience Centre, University of Jyväskylä, Jyväskylä 40014, Finland

Manu Lahtinen – Department of Chemistry, University of Jyväskylä, Jyväskylä 40014, Finland; orcid.org/0000-0001-5561-3259

Complete contact information is available at: <https://pubs.acs.org/doi/10.1021/acs.cgd.2c01351>

Author Contributions

The manuscript was written jointly and based on contributions from all authors. All authors have given approval to the final version of the manuscript.

Notes

The authors declare no competing financial interest.

■ ACKNOWLEDGMENTS

The Academy of Finland (A.V., Grant nos. 314343 and 335600 and J.O.M., Grant nos. 315829, 320015, and 345484) and the University of Jyväskylä are gratefully acknowledged for financial support. The authors thank Spec. Lab. Tech. Mirja Lahtiperä and Dr. Elina Kalenius for their work with mass spectrometry. We are also grateful to Prof. Kari Rissanen for his support and suggestions for the research. The CSC-IT Centre for Science in Finland, the Finnish Grid and Cloud Infrastructure (persistent identifier urn:nbn:fi:research-infras-2016072533) and Prof. H. M. Tuononen (University of Jyväskylä) are acknowledged for providing computational resources for the project.

■ REFERENCES

- (1) Desiraju, G. R.; Ho, P.; Kloo, L.; Legon, A. C.; Marquardt, R.; Metrangolo, P.; Politzer, P.; Resnati, G.; Rissanen, K. Definition of the Halogen Bond (IUPAC Recommendations 2013). *Pure Appl. Chem.* **2013**, *85*, 1711–1713.
- (2) Colin, J. J. Sur Quelques Combinaisons de l'Iode. *Ann. Chim. (Paris, Fr.)* **1814**, *91*, 252–272.
- (3) Guthrie, F. XXVIII.-On the iodide of iodammonium. *J. Chem. Soc.* **1863**, *16*, 239–244.
- (4) Legon, A. C. π -Electron "Donor-Acceptor" Complexes B...ClF and the Existence of the "Chlorine Bond". *Chem.—Eur. J.* **1998**, *4*, 1890–1897.
- (5) Legon, A. C. Prereactive Complexes of Dihalogens XY with Lewis Bases B in the Gas Phase: A Systematic Case for the Halogen Analogue B...XY of the Hydrogen Bond B...HX. *Angew. Chem., Int. Ed.* **1999**, *38*, 2686–2714.
- (6) Amico, V.; Meille, S. V.; Corradi, E.; Messina, M. T.; Resnati, G. Perfluorocarbon–Hydrocarbon Self-Assembling. 1D Infinite Chain Formation Driven by Nitrogen...Iodine Interactions. *J. Am. Chem. Soc.* **1998**, *120*, 8261–8262.
- (7) Corradi, E.; Meille, S. V.; Messina, M. T.; Metrangolo, P.; Resnati, G. Halogen Bonding versus Hydrogen Bonding in Driving Self-Assembly Processes. *Angew. Chem., Int. Ed.* **2000**, *39*, 1782–1786.
- (8) Metrangolo, P.; Resnati, G. Halogen Bonding: A Paradigm in Supramolecular Chemistry. *Chem.—Eur. J.* **2001**, *7*, 2511–2519.
- (9) Peuronen, A.; Valkonen, A.; Kortelainen, M.; Rissanen, K.; Lahtinen, M. Halogen Bonding-Based "Catch and Release": Reversible Solid-State Entrapment of Elemental Iodine with Monoalkylated DABCO Salts. *Cryst. Growth Des.* **2012**, *12*, 4157–4169.
- (10) Troff, R. W.; Mäkelä, T.; Topić, F.; Valkonen, A.; Raatikainen, K.; Rissanen, K. Alternative Motifs for Halogen Bonding. *Eur. J. Org. Chem.* **2013**, *2013*, 1617–1637.
- (11) Nizhnik, Y. P.; Sons, A.; Zeller, M.; Rosokha, S. V. Effects of Supramolecular Architecture on Halogen Bonding between Diiodine

- and Heteroaromatic *N*-Oxides. *Cryst. Growth Des.* **2018**, *18*, 1198–1207.
- (12) Topić, F.; Rissanen, K. Systematic Construction of Ternary Cocrystals by Orthogonal and Robust Hydrogen and Halogen Bonds. *J. Am. Chem. Soc.* **2016**, *138*, 6610–6616.
- (13) Puttreddy, R.; Topić, F.; Valkonen, A.; Rissanen, K. Halogen-Bonded Co-Crystals of Aromatic *N*-Oxides: Polydentate Acceptors for Halogen and Hydrogen Bonds. *Crystals* **2017**, *7*, 214.
- (14) Torubaev, Y. V.; Skabitskiy, I. V.; Rusina, P.; Pasynskii, A. A.; Rai, D. K.; Singh, A. Organometallic Halogen Bond Acceptors: Directionality, Hybrid Cocrystal Precipitation, and Blueshifted CO Ligand Vibrational Band. *CrystEngComm* **2018**, *20*, 2258–2266.
- (15) Nicolas, I.; Barrière, F.; Jeannin, O.; Fourmigué, M. Sequential Halogen Bonding with Ditopic Donors: σ -Hole Evolutions upon Halogen Bond Formation. *Cryst. Growth Des.* **2016**, *16*, 2963–2971.
- (16) Stilinović, V.; Horvat, G.; Hrenar, T.; Nemec, V.; Cinčić, D. Halogen and Hydrogen Bonding between (*N*-Halogeno)-Succinimides and Pyridine Derivatives in Solution, the Solid State and In Silico. *Chem.—Eur. J.* **2017**, *23*, 5244–5257.
- (17) Puttreddy, R.; Rautiainen, J. M.; Mäkelä, T.; Rissanen, K. Strong $N\cdots O\cdots N$ Halogen Bonds: A Comprehensive Study on *N*-Halosaccharin Pyridine *N*-Oxide Complexes. *Angew. Chem., Int. Ed.* **2019**, *58*, 18610–18618.
- (18) Turunen, L.; Warzok, U.; Puttreddy, R.; Beyeh, N. K.; Schalley, C. A.; Rissanen, K. [$N\cdots I\cdots N$] Halogen-Bonded Dimeric Capsules from Tetrakis(3-pyridyl)ethylene Cavitands. *Angew. Chem., Int. Ed.* **2016**, *55*, 14033–14036.
- (19) Turunen, L.; Warzok, U.; Schalley, C. A.; Rissanen, K. Nano-sized I12L6 Molecular Capsules Based on the [$N\cdots I\cdots N$] Halogen Bond. *Chem* **2017**, *3*, 861–869.
- (20) Turunen, L.; Peuronen, A.; Forsblom, S.; Kalenius, E.; Lahtinen, M.; Rissanen, K. Tetrameric and Dimeric [$N\cdots I\cdots N$] Halogen-Bonded Supramolecular Cages. *Chem.—Eur. J.* **2017**, *23*, 11714–11718.
- (21) Vanderkooy, A.; Gupta, A. K.; Földes, T.; Lindblad, S.; Orthaber, A.; Pápai, I.; Erdélyi, M. Halogen Bonding Helicates Encompassing Iodonium Cations. *Angew. Chem., Int. Ed.* **2019**, *58*, 9012–9016.
- (22) Turunen, L.; Erdélyi, M. Halogen Bonds of Halonium Ions. *Chem. Soc. Rev.* **2020**, *49*, 2688–2700.
- (23) Cavallo, G.; Metrangolo, P.; Milani, R.; Pilati, T.; Priimagi, A.; Resnati, G.; Terraneo, G. The Halogen Bond. *Chem. Rev.* **2016**, *116*, 2478–2601.
- (24) $R_{XB} = d(D\cdots A)/(R_D + R_A)$, where R_D and R_A are the van der Waals radii of D and A atoms; $\angle_{XB} = C-D\cdots A$ angle.
- (25) Hedidi, M.; Maillard, J.; Erb, W.; Lassagne, F.; Halauko, Y. S.; Ivashkevich, O. A.; Matulis, V. E.; Roisnel, T.; Dorcet, V.; Hamzé, M.; Fajloun, Z.; Baratte, B.; Ruchaud, S.; Bach, S.; Bentabed-Ababsa, G.; Mongin, F. Fused Systems Based on 2-Aminopyrimidines: Synthesis Combining Deprotolithiation-in situ Zincation with *N*-Arylation Reactions and Biological Properties. *Eur. J. Org. Chem.* **2017**, *2017*, 5903–5915.
- (26) Tsunobuchi, Y.; Kaneko, S.; Nakabayashi, K.; Ohkoshi, S. I. High Thermal Durability of Water-Free Copper-Octacyanotungsten-Based Magnets Containing Halogen Bonds. *Cryst. Growth Des.* **2011**, *11*, 5561–5566.
- (27) Chevallier, F.; Halauko, Y. S.; Pecceu, C.; Nassar, I. F.; Dam, T. U.; Roisnel, T.; Matulis, V. E.; Ivashkevich, O. A.; Mongin, F. *N*-Aryl Pyrazoles: DFT Calculations of CH Acidity and Deprotonative Metallation Using a Combination of Lithium and Zinc Amides. *Org. Biomol. Chem.* **2011**, *9*, 4671–4684.
- (28) Foyle, E. M.; White, N. G. Anion Templated Crystal Engineering of Halogen Bonding Tripodal Tris(Halopyridinium) Compounds. *CrystEngComm* **2020**, *22*, 2526–2536.
- (29) Zhang, H.; Toy, P. H. Halogen Bond-Catalyzed Friedel–Crafts Reactions of Furans Using a 2,2'-Bipyridine-Based Catalyst. *Adv. Synth. Catal.* **2021**, *363*, 215–221.
- (30) Fotović, L.; Stilinović, V. Halogen Bonding in *N*-Alkyl-3-Halogenopyridinium Salts. *Crystals* **2021**, *11*, 1240.
- (31) Fotović, L.; Bedekovic, N.; Stilinovic, V. Evaluation of Halogenopyridinium Cations as Halogen Bond Donors. *Cryst. Growth Des.* **2021**, *21*, 6889–6901.
- (32) Fotović, L.; Bedeković, N.; Stilinović, V. Isostructural Halogen Exchange and Halogen Bonds: The Case of *N*-(4-Halogenobenzyl)-3-Halogenopyridinium Halogenides. *Cryst. Growth Des.* **2022**, *22*, 1333–1344.
- (33) Raatikainen, K.; Cametti, M.; Rissanen, K. The Subtle Balance of Weak Supramolecular Interactions: The Hierarchy of Halogen and Hydrogen Bonds in Haloanilinium and Halopyridinium Salts. *Beilstein J. Org. Chem.* **2010**, *6*, 4–13.
- (34) Riel, A. M. S.; Decato, D. A.; Sun, J.; Massena, C. J.; Jessop, M. J.; Berryman, O. B. The Intramolecular Hydrogen Bonded-Halogen Bond: A New Strategy for Preorganization and Enhanced Binding. *Chem. Sci.* **2018**, *9*, 5828–5836.
- (35) Derossi, S.; Brammer, L.; Hunter, C. A.; Ward, M. D. Halogen Bonded Supramolecular Assemblies of $[Ru(bipy)(CN)_4]^{2-}$ Anions and *N*-Methyl-Halopyridinium Cations in the Solid State and in Solution. *Inorg. Chem.* **2009**, *48*, 1666–1677.
- (36) Ormond-Prout, J. E.; Smart, P.; Brammer, L. Cyanometallates as Halogen Bond Acceptors. *Cryst. Growth Des.* **2012**, *12*, 205–216.
- (37) Amendola, V.; Bergamaschi, G.; Boiocchi, M.; Fusco, N.; La Rocca, M. V.; Linati, L.; Lo Presti, E.; Mella, M.; Metrangolo, P.; Miljkovic, A. Novel Hydrogen- and Halogen-Bonding Anion Receptors Based on 3-Iodopyridinium Units. *RSC Adv.* **2016**, *6*, 67540–67549.
- (38) Groom, C. R.; Allen, F. H. The Cambridge Structural Database in Retrospect and Prospect. *Angew. Chem., Int. Ed.* **2014**, *53*, 662–671.
- (39) Valkonen, A.; Chukhlieb, M.; Moilanen, J.; Tuononen, H. M.; Rissanen, K. Halogen and Hydrogen Bonded Complexes of 5-Iodouracil. *Cryst. Growth Des.* **2013**, *13*, 4769–4775.
- (40) Beyeh, N. K.; Valkonen, A.; Bhowmik, S.; Pan, F.; Rissanen, K. *N*-Alkyl Ammonium Resorcinarene Salts: Multivalent Halogen-Bonded Deep-Cavity Cavitands. *Org. Chem. Front.* **2015**, *2*, 340–345.
- (41) Happonen, L.; Rautiainen, J. M.; Valkonen, A. Halogen Bonding between Thiocarbonyl Compounds and 1,2- and 1,4-Diiodotetrafluorobenzenes. *Cryst. Growth Des.* **2021**, *21*, 3409–3419.
- (42) Mečiarová, M.; Toma, Š.; Loupy, A.; Horváth, B. Synthesis of Phosphonium Salts – Phosphine Structure and Inorganic Salts Effects. *Phosphorus, Sulfur Silicon Relat. Elem.* **2008**, *183*, 21–33.
- (43) COLLECT; Bruker AXS Inc.: Madison, Wisconsin, USA 2004.
- (44) Otwinowski, Z.; Minor, W. Processing of X-Ray Diffraction Data Collected in Oscillation Mode. *Methods Enzymol.* **1997**, *276*, 306–326.
- (45) *CrysAlisPro*; Rigaku Oxford Diffraction: Oxford, 2015.
- (46) Burla, M. C.; Caliendo, R.; Carrozzini, B.; Cascarano, G. L.; Cuocci, C.; Giacovazzo, C.; Mallamo, M.; Mazzzone, A.; Polidori, G. Crystal structure determination and refinement via SIR2014. *J. Appl. Crystallogr.* **2015**, *48*, 306–309.
- (47) Sheldrick, G. M. Crystal structure refinement with SHELXL. *Acta Crystallogr., Sect. C: Struct. Chem.* **2015**, *71*, 3–8.
- (48) SADABS; Bruker AXS Inc.: Madison, Wisconsin, USA 2012.
- (49) Macrae, C. F.; Sovago, I.; Cottrell, S. J.; Galek, P. T. A.; McCabe, P.; Pidcock, E.; Platings, M.; Shields, G. P.; Stevens, J. S.; Towler, M.; Wood, P. A. Mercury 4.0: From Visualization to Analysis, Design and Prediction. *J. Appl. Crystallogr.* **2020**, *53*, 226–235.
- (50) Degen, T.; Sadki, M.; Bron, E.; König, U.; Nénert, G. The HighScore suite. *Powder Diffr.* **2014**, *29*, S13–S18.
- (51) ICDD-PDF4+ (Release 2020); International Centre for Diffraction Data: Newtown Square, Pennsylvania, USA, 2020.
- (52) Ernzerhof, M.; Scuseria, G. E. Assessment of the Perdew–Burke–Ernzerhof Exchange–Correlation Functional. *J. Chem. Phys.* **1999**, *110*, 5029–5036.
- (53) Adamo, C.; Barone, V. Toward Reliable Density Functional Methods without Adjustable Parameters: The PBE0 Model. *J. Chem. Phys.* **1999**, *110*, 6158–6170.

- (54) Becke, A. D. Density-Functional Exchange-Energy Approximation with Correct Asymptotic Behavior. *Phys. Rev. A: At., Mol., Opt. Phys.* **1988**, *38*, 3098–3100.
- (55) Becke, A. D. Density-functional thermochemistry. III. The role of exact exchange. *J. Chem. Phys.* **1993**, *98*, 5648–5652.
- (56) Zhao, Y.; Truhlar, D. G. The M06 Suite of Density Functionals for Main Group Thermochemistry, Thermochemical Kinetics, Noncovalent Interactions, Excited States, and Transition Elements: Two New Functionals and Systematic Testing of Four M06-Class Functionals and 12 Other Functionals. *Theor. Chem. Acc.* **2008**, *120*, 215–241.
- (57) Chai, J.-D.; Head-Gordon, M. Long-Range Corrected Hybrid Density Functionals with Damped Atom-Atom Dispersion Corrections. *Phys. Chem. Chem. Phys.* **2008**, *10*, 6615–6620.
- (58) Weigend, F.; Ahlrichs, R. Balanced Basis Sets of Split Valence, Triple Zeta Valence and Quadruple Zeta Valence Quality for H to Rn: Design and Assessment of Accuracy. *Phys. Chem. Chem. Phys.* **2005**, *7*, 3297–3305.
- (59) Pritchard, B. P.; Altarawy, D.; Didier, B.; Gibson, T. D.; Windus, T. L. New Basis Set Exchange: An Open, Up-to-Date Resource for the Molecular Sciences Community. *J. Chem. Inf. Model.* **2019**, *59*, 4814–4820.
- (60) Peterson, K. A.; Figgen, D.; Goll, E.; Stoll, H.; Dolg, M. Systematically Convergent Basis Sets with Relativistic Pseudopotentials. II. Small-Core Pseudopotentials and Correlation Consistent Basis Sets for the Post-d Group 16-18 Elements. *J. Chem. Phys.* **2003**, *119*, 11113–11123.
- (61) Grimme, S.; Antony, J.; Ehrlich, S.; Krieg, H. A Consistent and Accurate Ab Initio Parametrization of Density Functional Dispersion Correction (DFT-D) for the 94 Elements H-Pu. *J. Chem. Phys.* **2010**, *132*, 154104.
- (62) Grimme, S.; Ehrlich, S.; Goerigk, L. Effect of the Damping Function in Dispersion Corrected Density Functional Theory. *J. Comput. Chem.* **2011**, *32*, 1456–1465.
- (63) Frisch, M. J.; Trucks, G. W.; Schlegel, H. B.; Scuseria, G. E.; Robb, M. A.; Cheeseman, J. R.; Scalmani, G.; Barone, V.; Petersson, G. A.; Nakatsuji, H.; Li, X.; Caricato, M.; Marenich, A. v.; Bloino, J.; Janesko, B. G.; Gomperts, R.; Mennucci, B.; Hratchian, H. P.; Ortiz, J. v.; Izmaylov, A. F.; Sonnenberg, J. L.; Williams-Young, D.; Ding, F.; Lipparini, F.; Egidi, F.; Goings, J.; Peng, B.; Petrone, A.; Henderson, T.; Ranasinghe, D.; Zakrzewski, V. G.; Gao, J.; Rega, N.; Zheng, G.; Liang, W.; Hada, M.; Ehara, M.; Toyota, K.; Fukuda, R.; Hasegawa, J.; Ishida, M.; Nakajima, T.; Honda, Y.; Kitao, O.; Nakai, H.; Vreven, T.; Throssell, K.; Montgomery, J. A., Jr.; Peralta, J. E.; Ogliaro, F.; Bearpark, M. J.; Heyd, J. J.; Brothers, E. N.; Kudin, K. N.; Staroverov, V. N.; Keith, T. A.; Kobayashi, R.; Normand, J.; Raghavachari, K.; Rendell, A. P.; Burant, J. C.; Iyengar, S. S.; Tomasi, J.; Cossi, M.; Millam, J. M.; Klene, M.; Adamo, C.; Cammi, R.; Ochterski, J. W.; Martin, R. L.; Morokuma, K.; Farkas, O.; Foresman, J. B.; Fox, D. J. *Gaussian 16*; Gaussian Inc.: Wallingford, Connecticut, USA, 2016;.
- (64) Glendening, E. D.; Badenhoop, J. K.; Reed, A. E.; Carpenter, J. E.; Bohmann, J. A.; Morales, C. M.; Karafiloglou, P.; Landis, C. R.; Weinhold, F. *NBO 7.0*; Theoretical Chemistry Institute, University of Wisconsin: Madison, Wisconsin, USA, 2018;.
- (65) Dovesi, R.; Erba, A.; Orlando, R.; Zicovich-Wilson, C. M.; Civalieri, B.; Maschio, L.; Rérat, M.; Casassa, S.; Baima, J.; Salustro, S.; Kirtman, B. Quantum-Mechanical Condensed Matter Simulations with CRYSTAL. *Wiley Interdiscip. Rev.: Comput. Mol. Sci.* **2018**, *8*, No. e1360.
- (66) Laun, J.; Vilela Oliveira, D.; Bredow, T. Consistent Gaussian Basis Sets of Double- and Triple-Zeta Valence with Polarization Quality of the Fifth Period for Solid-State Calculations. *J. Comput. Chem.* **2018**, *39*, 1285–1290.
- (67) Peintinger, M. F.; Oliveira, D. V.; Bredow, T. Consistent Gaussian Basis Sets of Triple-Zeta Valence with Polarization Quality for Solid-State Calculations. *J. Comput. Chem.* **2013**, *34*, 451–459.
- (68) Boys, S. F.; Bernardi, F. The calculation of small molecular interactions by the differences of separate total energies. Some procedures with reduced errors. *Mol. Phys.* **1970**, *19*, 553–566.
- (69) Simon, S.; Duran, M.; Dannenberg, J. J. How does basis set superposition error change the potential surfaces for hydrogen-bonded dimers? *J. Chem. Phys.* **1996**, *105*, 11024–11031.
- (70) Powell, J.; Horvath, M. J.; Lough, A.; Phillips, A.; Brunet, J. Synthetic and single-crystal X-ray diffraction studies of CH₂I₂ and aryl iodide complexes of silver carboxylates and β -diketonates. *J. Chem. Soc., Dalton Trans.* **1998**, 637–646.
- (71) Lasanta, T.; Olmos, M. E.; Laguna, A.; López-de-Luzuriaga, J. M.; Naumov, P. Making the Golden Connection: Reversible Mechanochemical and Vapochemical Switching of Luminescence from Bimetallic Gold-Silver Clusters Associated through Auophilic Interactions. *J. Am. Chem. Soc.* **2011**, *133*, 16358–16361.
- (72) Aubert, E.; Abboud, M.; Doudouh, A.; Durand, P.; Peluso, P.; Ligresti, A.; Vigolo, B.; Cossu, S.; Pale, P.; Mamane, V. Silver(i) coordination polymers with 3,3',5,5'-tetrasubstituted 4,4'-bipyridine ligands: towards new porous chiral materials. *RSC Adv.* **2017**, *7*, 7358–7367.
- (73) Kniep, F.; Walter, S. M.; Herdtweck, E.; Huber, S. M. 4,4'-Azobis(halopyridinium) Derivatives: Strong Multidentate Halogen-Bond Donors with a Redox-Active Core. *Chem.—Eur. J.* **2012**, *18*, 1306–1310.
- (74) Fotović, F.; Stilić, V. Halogenide anions as halogen and hydrogen bond acceptors in iodopyridinium halogenides. *CrystEngComm* **2020**, *22*, 4039–4046.
- (75) Jakupc, N.; Fotović, L.; Stilić, V. The effect of halogen bonding on protonated hexacyanoferrate networks in hexacyanoferrates of halogenopyridines. *CrystEngComm* **2020**, *22*, 8142–8150.
- (76) Riel, A. M. S.; Decato, D. A.; Sun, J.; Berryman, O. B. Halogen bonding organocatalysis enhanced through intramolecular hydrogen bonds. *Chem. Commun.* **2022**, *58*, 1378–1381.
- (77) Decato, D. A.; Riel, A. M. S.; May, J. H.; Bryantsev, V. S.; Berryman, O. B. Theoretical, Solid-State, and Solution Quantification of the Hydrogen Bond-Enhanced Halogen Bond. *Angew. Chem., Int. Ed.* **2021**, *60*, 3685–3692.
- (78) Jones, P. G.; Cots Carrasquer, B. C.; Zerbe, E.-M. 1-Carboxymethyl-3-iodo-1-pyridinium-iodide-(3-iodo-1-pyridinio)-acetate (1/1/1). *Acta Crystallogr., Sect. E: Struct. Rep. Online* **2005**, *61*, o895.
- (79) Weiss, R.; Golisano, T.; Pale, P.; Mamane, V. Insight into the Modes of Activation of Pyridinium and Bipyridinium Salts in Non-Covalent Organocatalysis. *Adv. Synth. Catal.* **2021**, *363*, 4779–4788.
- (80) Chapman, M. R.; Kwan, M. H. T.; King, G. E.; Kyffin, B. A.; Blacker, A. J.; Willans, C. E.; Nguyen, B. N. Rapid, metal-free and aqueous synthesis of imidazo[1,2-a]pyridine under ambient conditions. *Green Chem.* **2016**, *18*, 4623–4627.
- (81) Engelage, E.; Hijazi, H.; Gartmann, M.; Chamoreau, L.-M.; Schöllhorn, B.; Huber, S. M.; Fave, C. Towards redox-switchable organocatalysts based on bidentate halogen bond donors. *Phys. Chem. Chem. Phys.* **2021**, *23*, 4344–4352.
- (82) Bartashevich, E. V.; Stash, A. I.; Batalov, V. I.; Yushina, I. D.; Drebuschak, T. N.; Boldyreva, E. v.; Tsirelson, V. G. The Staple Role of Hydrogen and Halogen Bonds in Crystalline (E)-8-((2,3-Diiodo-4-(quinolin-8-ylthio)but-2-en-1-yl)thio)quinolin-1-ium Triiodide. *Struct. Chem.* **2016**, *27*, 1553–1560.
- (83) Forni, A.; Franchini, D.; Dapiaggi, F.; Pieraccini, S.; Sironi, M.; Scilabra, P.; Pilati, T.; Petko, K. I.; Resnati, G.; Yagupol'kii, Y. L. Featuring 1···N Halogen Bond and Weaker Interactions in Iodoperfluoroalkylimidazoles: An Experimental and Theoretical Charge Density Study. *Cryst. Growth Des.* **2019**, *19*, 1621–1631.
- (84) Bol'shakov, O. I.; Yushina, I. D.; Bartashevich, E. V.; Nelyubina, Y. V.; Aysin, R. R.; Rakitin, O. A. Asymmetric Triiodide-Diiodine Interactions in the Crystal of (Z)-4-Chloro-5-((2-((4-chloro-5H-1,2,3-dithiazol-5-ylidene)amino)phenyl)amino)-1,2,3-dithiazol-1-ium Oligoiodide. *Struct. Chem.* **2017**, *28*, 1927–1934.
- (85) Yushina, I. D.; Masunov, A. E.; Lopez, D.; Dyakov, A. A.; Bartashevich, E. V. Toward First-Principles Design of Organic Nonlinear Optical Materials: Crystal Structure Prediction and Halogen Bonding Impact on Hyperpolarizabilities of 2-Iodo-3-Hydroxypyridine. *Cryst. Growth Des.* **2018**, *18*, 5069–5079.

(86) Schaub, T. A.; Sure, R.; Hampel, F.; Grimme, S.; Kivala, M. Quantum Chemical Dissection of the Shortest $\text{P}=\text{O}\cdots\text{I}$ Halogen Bond: The Decisive Role of Crystal Packing Effects. *Chem.—Eur. J.* **2017**, *23*, 5687–5691.

(87) Masunov, A. E.; Wiratmo, M.; Dyakov, A. A.; Matveychuk, Y. V.; Bartashevich, E. V. Virtual Tensile Test for Brittle, Plastic, and Elastic Polymorphs of 4-Bromophenyl 4-Bromobenzoate. *Cryst. Growth Des.* **2020**, *20*, 6093–6100.

(88) Masunov, A. E.; Torres, K.; Dyakov, A. A.; Yushina, I. D.; Bartashevich, E. V. First-Principles Crystal Engineering of Nonlinear Optical Materials. II. Effect of Halogen Bonds on the Structure and Properties of Triiodobenzenes. *J. Phys. Chem. C* **2018**, *122*, 22622–22631.

(89) Kozuch, S.; Martin, J. M. L. Halogen Bonds: Benchmarks and Theoretical Analysis. *J. Chem. Theory Comput.* **2013**, *9*, 1918–1931.

(90) Portalone, G.; Moilanen, J. O.; Tuononen, H. M.; Rissanen, K. Role of Weak Hydrogen Bonds and Halogen Bonds in 5-Halo-1,3-dimethyluracils and Their Cocrystals—A Combined Experimental and Computational Study. *Cryst. Growth Des.* **2016**, *16*, 2631–2639.

Recommended by ACS

Stability and Mechanical Properties of Darunavir Isostructural Solvates: An Experimental and Computational Study

Kaxi Yu, Xiurong Hu, *et al.*

FEBRUARY 28, 2023
CRYSTAL GROWTH & DESIGN

READ 

Equations of State and Crystal Structures of KCaPO_4 , KSrPO_4 , and $\text{K}_2\text{Ce}(\text{PO}_4)_2$ under High Pressure: Discovery of a New Polymorph of KCaPO_4

Daniel Errandonea, Frederico G. Alabarse, *et al.*

FEBRUARY 28, 2023
CRYSTAL GROWTH & DESIGN

READ 

Co-Former Selection for Coamorphous Amino Acid/Spirolactone Formulations and Exploration of the Amorphization Kinetics of Systems

Maolin Li, Junbo Gong, *et al.*

FEBRUARY 16, 2023
CRYSTAL GROWTH & DESIGN

READ 

Study on the Formation Mechanism of Acetaldehyde during the Low-Temperature Oxidation of Coal

Junfeng Wang, Yulong Zhang, *et al.*

DECEMBER 23, 2022
ACS OMEGA

READ 

Get More Suggestions >